

# CO<sub>2</sub> Reduction for C<sub>2</sub>+ in Seawater Using a Graphitic Frustrated Lewis Pair Catalyst

Tae-Hyuk Kwon (✉ [kwon90@unist.ac.kr](mailto:kwon90@unist.ac.kr))

Ulsan National Institute of Science and Technology <https://orcid.org/0000-0002-1633-6065>

Hyun-Tak Kim

Ulsan National Institute of Science and Technology

Jaehyun Park

Ulsan National Institute of Science and Technology

Jinhong Mun

Ulsan National Institute of Science and Technology

HyeonOh Shin

Ulsan National Institute of Science and Technology

Deok-Ho Roh

Ulsan National Institute of Science and Technology

Junhyeok Kwon

Ulsan National Institute of Science and Technology

Sungtae Kim

Ulsan National Institute of Science and Technology

Geunsik Lee

Ulsan National Institute of Science and Technology <https://orcid.org/0000-0002-2477-9990>

Seok Ju Kang

Columbia University <https://orcid.org/0000-0002-9921-6674>

---

## Article

**Keywords:** Ocean acidification, Anthropogenic CO<sub>2</sub> emissions, CO<sub>2</sub> Reduction Battery System, Molecular Design Strategy

**Posted Date:** November 21st, 2020

**DOI:** <https://doi.org/10.21203/rs.3.rs-98223/v1>

**License:**   This work is licensed under a Creative Commons Attribution 4.0 International License.

[Read Full License](#)

---

# CO<sub>2</sub> Reduction for C<sub>2+</sub> in Seawater Using a Graphitic Frustrated Lewis Pair Catalyst

Hyun-Tak Kim<sup>1,3†</sup>, Jaehyun Park<sup>2,3†</sup>, Jinhong Mun<sup>1,3†</sup>, HyeonOh Shin<sup>1,3</sup>, Deok-Ho Roh<sup>1,3</sup>, Junhyeok Kwon<sup>1,3</sup>, Sungtae Kim<sup>1,3</sup>, Geunsik Lee<sup>1,3\*</sup>, Seok Ju Kang<sup>2,3\*</sup>, and Tae-Hyuk Kwon<sup>1,3\*</sup>

<sup>1</sup>Department of Chemistry, School of Natural Science, Ulsan National Institute of Science and Technology (UNIST), Ulsan 44919, Republic of Korea

<sup>2</sup>Department of Energy Engineering, School of Energy and Chemical Engineering, Ulsan National Institute of Science and Technology (UNIST), Ulsan 44919, Republic of Korea

<sup>3</sup>Center for Wave Energy Materials, Ulsan National Institute of Science and Technology (UNIST), Ulsan 44919, Republic of Korea

† These authors contributed equally to this work.

## Corresponding Author

\* E-mail: [gslee@unist.ac.kr](mailto:gslee@unist.ac.kr), [sjkang@unist.ac.kr](mailto:sjkang@unist.ac.kr), [kwon90@unist.ac.kr](mailto:kwon90@unist.ac.kr)

1 **Ocean acidification due to the absorption of 40% of the world's anthropogenic CO<sub>2</sub> emissions**  
2 **severely affects the faltering marine ecosystem and the economy. However, there are few reports**  
3 **on reducing CO<sub>2</sub> dissolved in seawater. Herein, we introduce an electrochemical CO<sub>2</sub> reduction**  
4 **battery system for use in seawater with a graphitic frustrated Lewis pair catalytic cathode doped**  
5 **with boron and nitrogen (BN-GFLP). BN-GFLP converts CO<sub>2</sub> dissolved in seawater to multi-**  
6 **carbon (C<sub>2+</sub>) products during the discharge process, thus increasing the pH of intentionally**  
7 **acidified seawater from 6.4 to 8.0 with more than 87% Faradaic efficiency. In computational**  
8 **chemistry and spectroscopy, BN-GFLP binds CO<sub>2</sub> in a unique manner that enables exothermic**  
9 **C–C coupling pathway to deliver 95% selectivity for valuable C<sub>2+</sub> products. Based on our results,**  
10 **we suggest a molecular design strategy for next-generation CO<sub>2</sub> reduction catalysts for both green**  
11 **oceans and the atmosphere.**

1 Marine life is gradually dying due to increasing amounts of carbon dioxide (CO<sub>2</sub>) in the atmosphere  
2 caused by human activity. As the ocean absorbs ~40% of the world's anthropogenic CO<sub>2</sub> emissions, ocean  
3 acidity has increased by ~26% since the pre-industrial era, a trend that is expected to continue<sup>1-4</sup>. The  
4 impact of ocean acidification adversely affects marine calcifying organisms, such as coral, plankton,  
5 shells, and skeletons, resulting in a drastic faltering of the marine food chain and the economy<sup>1-4</sup>.  
6 Therefore, the reduction of CO<sub>2</sub> in the seawater environment is a major problem that needs to be solved  
7 by mankind as it can affect climate change, employment, and food security. However, most CO<sub>2</sub>  
8 mitigation efforts have focused on the atmosphere and not directly on the ocean<sup>5-13</sup>. For example,  
9 electrochemical CO<sub>2</sub> reduction (CO<sub>2</sub>R) progressed significantly over the past decade in terms of the  
10 development and understanding of various catalytic materials, such as precious metals<sup>6</sup>, base metals<sup>7</sup>,  
11 metal oxides<sup>8</sup>, covalent organic frameworks<sup>9</sup>, and metal-organic frameworks<sup>10</sup>. Among the developed  
12 electrocatalysts, copper-based electrocatalysts have the remarkable propensity to produce valuable multi-  
13 carbon (C<sub>2+</sub>) products, such as ethylene and ethanol, from CO<sub>2</sub>R<sup>5,11-13</sup>. However, it is difficult to use  
14 existing CO<sub>2</sub>R electrocatalysts in seawater because of their complexity and the presence of undesirable  
15 ionic species<sup>14</sup>. Specifically, Ca<sup>2+</sup> in seawater directly decreases the CO<sub>2</sub>R activity of metallic catalysts  
16 due to the precipitation of CaCO<sub>3</sub> on their surfaces<sup>14,15</sup>. Only a few reports have focused on using seawater  
17 as an electrolyte, with a poor Faradaic efficiency (FE) of 36% being reported<sup>14,16</sup>. Nevertheless, seawater  
18 can be an extremely attractive electrolyte for CO<sub>2</sub>R because it is abundant, can function as a sink for CO<sub>2</sub>,  
19 and has an inherently high ionic conductivity<sup>14,17,18</sup>. Therefore, systems for CO<sub>2</sub>R in seawater are urgently  
20 needed for the marine ecosystem.

21 With this aim, we introduce a new CO<sub>2</sub>R battery in seawater (CBS) system comprising a graphitic  
22 frustrated Lewis pair (GFLP) cathode, a Na metal anode, and natural seawater as the electrolyte, which  
23 can drastically recover the pH of seawater during discharging. In general, the properties of frustrated  
24 Lewis pairs (FLPs) are ideal for capturing CO<sub>2</sub> because the relatively constrained Lewis acid (LA) and  
25 Lewis base (LB) pair strongly binds to CO<sub>2</sub><sup>19-22</sup>. Therefore, we modified the FLP system for seawater

1 applications using a carbon nanomaterial with an immobilised LA and LB pair on a graphitic framework,  
2 which we refer to as ‘GFLP’. The  $sp^2$ -hybridised graphitic framework of GFLP can donate  $\pi$ -electrons to  
3 FLP sites, thereby enhancing the catalytic activity and electrochemical stability in seawater<sup>23</sup>. Graphene  
4 nanopowder (GN) was used as the carbon precursor owing to its high surface area and electrical  
5 conductivity, whereas boron (B) and nitrogen (N) were selected as the LA and LB, respectively.

## 6 **BN-GFLP synthesis and characterisation**

7 We introduce the sono-cavitation and nebulisation synthesis (SNS) method<sup>24</sup> for the synthesis of GFLP  
8 (Fig. 1a). A solution of GN and bis(pinacolato)diboron (a boron dopant) in *N*-methyl-2-pyrrolidone was  
9 passed through an ultrasonic nozzle using a syringe pump, which created vacuum bubbles inside the  
10 solution when high-frequency ultrasound (180 kHz) was applied (Fig. 1a). Acoustic cavitation creates  
11 extreme conditions inside the implodingly collapsing bubbles (temperature  $\approx 5000$  K, pressure  $\approx 1000$  bar,  
12 and heating and cooling rates  $>10^9$  K s<sup>-1</sup>)<sup>25</sup>, which is a well-known process in sonochemistry<sup>26</sup>. Such  
13 conditions permit various chemical reactions that are normally inaccessible<sup>25,27</sup>. The GN precursor in  
14 these bubbles can form ions or radicals that directly react with the boron dopant and even inert N<sub>2</sub> gas in  
15 a simple, fast, and continuous manner<sup>24</sup>. Using this approach, we synthesized B, N, and BN co-doped GN  
16 materials, denoted as B-GN, N-GN, and BN-GFLP, respectively, and their electrodes on a carbon felt  
17 substrate (more detailed synthesis conditions are described in the Methods).

18 High-resolution transmission electron microscopy images showed that the two-dimensional BN-GFLP  
19 structures contain substantial wrinkles and scrolls, which are characteristic of graphene (Supplementary  
20 Fig. 1). Energy-dispersive X-ray spectroscopy revealed clear and uniform distributions of B and N,  
21 implying that the LA and LB sites in BN-GFLP may be on the molecular scale (Supplementary Fig. 2).  
22 X-ray photoelectron spectroscopy (XPS) confirmed that the prepared carbon nanomaterials are doped at  
23 high heteroatom concentrations, i.e. 3.1 at% B in B-GN, 4.1 at% N in N-GN, and 6.8 at% B and 4.2 at%  
24 N in BN-GFLP (Fig. 1b). Furthermore, the heteroatom-doping contents of the GN materials can be  
25 controlled by the N<sub>2</sub> pressure (Supplementary Fig. 3) and concentration of the B dopant (Supplementary

1 Fig. 4) (details on the optimised processes are given in the Supplementary Information). The B 1s high-  
2 resolution spectrum of BN-GFLP was deconvoluted into four component peaks, revealing the presence  
3 of B–C (188.7 eV), sp<sup>2</sup>-C–B–N (189.8 eV), sp<sup>2</sup>-BN (191.5 eV), and B–O (193.1 eV) bonds  
4 (Supplementary Fig. 5a). The N 1s high-resolution spectrum of BN-GFLP also showed noticeable  
5 pyridinic (398.6 eV), pyrrolic (399.5 eV), and graphitic (401.2 eV) N peaks (Supplementary Fig. 5b).  
6 Although the SNS process randomly inserted heteroatoms into GN, three types of heteroatom  
7 configuration were present in the BN-GFLP structure according to XPS (Supplementary Fig. 5c). These  
8 heteroatom-doping characteristics were also evidenced by a higher D-to-G band Raman intensity ratio  
9 ( $I_D/I_G$ ) than that of the control GN (Supplementary Fig. 6). Furthermore, the heteroatom doped-GN  
10 materials exhibited paramagnetic properties below 10 K due to the presence of radical defects from the  
11 doped B and N, as determined by electron paramagnetic resonance spectroscopy (Fig. 1c). In contrast,  
12 bare GN is strongly diamagnetic, similar to graphite<sup>28,29</sup>. The radical defects in BN-GFLP contribute to  
13 accelerating the first CO<sub>2</sub> surface-adsorption step.

## 14 **Structural understanding of BN-GFLP**

15 The LA and LB in BN-GFLP were characterised by magic angle spinning nuclear magnetic resonance  
16 (MAS NMR) spectroscopy (Figs. 1d,e). Acidity was first determined by <sup>31</sup>P MAS NMR spectroscopy  
17 using the <sup>31</sup>P-trimethylphosphine (TMP)<sup>23,30</sup> phosphorus probe adsorbed on a BN-GFLP sample (Fig. 1d).  
18 A <sup>31</sup>P peak at 35.47 ppm was observed for BN-GFLP, which is attributable to the physical adsorption of  
19 TMP oxide (TMPO) on the BN-GFLP surface by the reaction of TMP with oxygen functional groups<sup>30–</sup>  
20 <sup>32</sup>. A <sup>31</sup>P peak at 55.04 ppm appeared when TMPO was chemisorbed at the LA boron sites of BN-GFLP  
21 (Fig. 1d), which corresponds to Lewis acidities in the 50–55 ppm range<sup>30–32</sup>. It is worth noting that weak  
22 Brønsted acid peaks for TMP-adsorbed BN-GFLP appear at –8.79 and –15.69 ppm<sup>30</sup>. Then, to determine  
23 basicity, pyrrole was used as the probe for <sup>1</sup>H MAS NMR spectroscopy (Fig. 1e)<sup>23,33,34</sup>. The intense peak  
24 at 5.95 ppm is assigned to the protons of aromatic pyrrole ring. Unlike the normal peak of NH group in  
25 pyrrole (8.26 ppm), the pyrrole adsorbed on the BN-GFLP sample exhibited a large <sup>1</sup>H chemical shift in

1 the shoulder peak at approximately 13.89 ppm owing to hydrogen bonding interactions<sup>33</sup> with the LB  
2 nitrogen in BN-GFLP (Fig. 1e). This result is similar to the chemical shifts observed in corresponding  
3 KX zeolites, which are known as super basic materials<sup>34</sup>. It is also noteworthy that the broadened peaks  
4 of the LA and LB sites in the <sup>31</sup>P and <sup>1</sup>H MAS NMR results are caused by the  $\pi$ -electron donating ability  
5 of the sp<sup>2</sup>-hybridised framework of BN-GFLP (Figs. 1d,e).

## 6 **Electrocatalytic CO<sub>2</sub>R activity of BN-GFLP in CBS system**

7 Then, we fabricated a gas-tight Swagelok-type CBS system consisting of a modified 2465-type coin cell  
8 comprising a BN-GFLP cathode, Na metal anode, natural seawater as the electrolyte, and superionic  
9 conductor membrane, which enables the formation of an aprotic electrolyte-based seawater hybrid  
10 system<sup>35</sup> (Supplementary Fig. 7). The CBS was connected to a pressure measuring system that  
11 consecutively measures the changes in inner CO<sub>2</sub> gas pressure during the discharge process. We then  
12 quantitatively verified the CO<sub>2</sub>R selectivity of BN-GFLP from the hydrogen evolution reaction (HER) in  
13 in situ experiments using a home-built differential electrochemical mass spectrometry (DEMS) system.  
14 The pressure decay of the Swagelok-type CBS cell filled with pure CO<sub>2</sub> gas was monitored during the  
15 electrochemical discharge process. Figures 2a and c show the galvanostatic discharge voltage profiles and  
16 the corresponding CO<sub>2</sub> reduction results, respectively, of the prepared catalytic electrodes at a fixed  
17 current density of 0.13 mA cm<sup>-2</sup>. The observed stable voltage plateau with a linear drop in consumed CO<sub>2</sub>  
18 gas revealed that the co-doped BN-GFLP delivered a lower CO<sub>2</sub> reduction overpotential and significantly  
19 enhanced CO<sub>2</sub> reduction performance compared with the GN, N-GN, and B-GN catalysts (Fig. 2a, red  
20 line). It should be noted that the single-heteroatom-doped B-GN catalyst showed high CO<sub>2</sub> reduction but  
21 a similar overpotential to that of the control (GN), whereas the N-GN single catalytic electrode had a  
22 lower overpotential but similar CO<sub>2</sub> consumption to that of the control. These results agree with the  
23 theoretical explanation that the LA enhances catalytic activity, whereas LB increases the reaction rate<sup>36</sup>.  
24 Therefore, BN-GFLP, with its FLP structure, increases CO<sub>2</sub>R efficiency through synergism between LA  
25 and LB. Notably, the physically mixed N-GN and B-GN showed different CO<sub>2</sub>R performance than that

1 shown by BN-GFLP (a detailed explanation of the mixed N-GN and B-GN is shown in Supplementary  
2 Fig. 8). The two-electrode Swagelok-type CBS system was also subjected to linear sweep voltammetry  
3 (LSV) under various gas atmospheres to further confirm CO<sub>2</sub>R selectivity versus HER (Figs. 2b,d). As  
4 shown in Fig. 2b, the LSV curves of BN-GFLP exhibited significant differences in onset potential for  
5 CO<sub>2</sub>R (2.6 V vs. Na/Na<sup>+</sup>) under CO<sub>2</sub> saturation and HER (1.7 V vs. Na/Na<sup>+</sup>) under Ar saturation in the  
6 seawater electrolyte. In particular, inner pressure decay and real-time DEMS measurements of the gas-  
7 tight Swagelok-type CBS system revealed that CO<sub>2</sub> was reduced at potentials up to 2.0 V and that H<sub>2</sub> gas  
8 was evolved from a sweep voltage of 1.8 V (Fig. 2d); these results are well matched with the onset  
9 potential for galvanostatic discharge (Fig. 2a) and LSV curves (Fig. 2b). Thus, we confirmed that BN-  
10 GFLP exhibits reliable CO<sub>2</sub>R selectivity versus HER.

11 We performed <sup>11</sup>B and <sup>15</sup>N NMR spectroscopy to validate the capacity of BN-GFLP to bind CO<sub>2</sub> (Figs.  
12 2e,f). Prior to CO<sub>2</sub> gas stimulus, BN-GFLP showed broad <sup>11</sup>B peaks due to inhomogeneous boron doping  
13 in the graphitic framework (Fig. 2e). In contrast, a remarkably intense <sup>11</sup>B signal at 27.58 ppm associated  
14 with BO bonds was observed for BN-GFLP with CO<sub>2</sub><sup>37</sup>. For <sup>15</sup>N NMR spectroscopy, <sup>15</sup>N urea was used  
15 as the <sup>15</sup>N dopant in BN-GFLP (synthesis details are given in the Methods). Without CO<sub>2</sub>, the <sup>15</sup>N NMR  
16 spectrum showed a broad peak at 64.41 ppm from <sup>15</sup>N in the graphitic framework of the BN-GFLP sample  
17 (Fig. 2f). In contrast, in BN-GFLP with CO<sub>2</sub>, two sharp peaks at 71.05 and 91.72 ppm appeared due to  
18 two possible N–C interaction modes (Fig. 2f, inset). We assumed that the bidentate coordination of N–C  
19 and B–O corresponded to the more downshifted peak (at 91.72 ppm) due to charge localisation effects,  
20 compared with monodentate N–C coordination (at 71.05 ppm)<sup>38</sup>. This hypothesis was supported by  
21 Raman spectroscopy (Supplementary Fig. 9), temperature programmed desorption (Supplementary Fig.  
22 10), and the subsequent computational study. These NMR results confirm that CO<sub>2</sub> adsorbs on BN-GFLP  
23 through boron binding as the LA to the oxygen of CO<sub>2</sub>, with nitrogen binding as the LB to the carbon<sup>21</sup>  
24 (Fig. 1a).

## 25 **Performance of CBS cell in anthropogenic acidified seawater**

1 For actual CO<sub>2</sub>R operation in a seawater environment, we fabricated the zig-type CBS cell shown in Fig.  
2 3a. The zig-type CBS cell with CO<sub>2</sub> bubbling provided sufficient electrical energy to operate a light-  
3 emitting diode (LED) device (Fig. 3b). In addition, to reflect natural ocean acidification by anthropogenic  
4 CO<sub>2</sub> emissions, we intentionally prepared CO<sub>2</sub>-saturated seawater by bubbling CO<sub>2</sub> for 2 h, resulting in a  
5 drastic decrease in pH to 6.4. This acidified seawater electrolyte was restored by the CO<sub>2</sub>R activity of the  
6 BN-GFLP cathode, resulting in a gradual increase in pH from 6.4 to 8.0 after 90 h of CBS discharging  
7 (Fig. 3c). The charge–discharge cycling stability of the CBS cell under a CO<sub>2</sub> atmosphere was well  
8 retained for 200 h with lower discharge–charge overpotentials than the GN catalyst (Fig. 3d).

9 The unusual multi-carbon liquid products (C<sub>2+</sub>), such as ethanol, *n*-propanol, and a small amount of  
10 methanol, from CO<sub>2</sub>R were collected and identified by electrospray ionisation mass spectrometry  
11 (Supplementary Fig. 11) and high-performance liquid chromatography (Supplementary Fig. 13). At 0.13  
12 mA cm<sup>-2</sup>, the total CO<sub>2</sub>R FE on BN-GFLP was 87.6% and selectivity for C<sub>2+</sub> (ethanol and *n*-propanol)  
13 was 95.0% in the seawater electrolyte (Supplementary Fig. 15). The detailed mechanism for C<sub>2+</sub> alcohol  
14 production from CO<sub>2</sub>R will be discussed in the computational chemistry study. Furthermore, during the  
15 CO<sub>2</sub>R process in seawater, calcite (CaCO<sub>3</sub>) precipitates in response to a local increase in pH, which is a  
16 major stability issue with metallic CO<sub>2</sub>R catalysts<sup>14,15</sup>. This calcification is generally related to the  
17 existence of Ca<sup>2+</sup> in seawater<sup>14</sup>. However, no CaCO<sub>3</sub> was detected on the surface of BN-GFLP in our  
18 CBS system, even after intentionally adding 0.5 M CaCl<sub>2</sub> to the seawater electrolyte; only C<sub>2+</sub> products  
19 were detected, similar to those observed in pure seawater (Supplementary Figs. 12, 13, and 15). Moreover,  
20 the dissolved CO<sub>2</sub> in seawater is converted at equilibrium into bicarbonate (HCO<sub>3</sub><sup>-</sup>) at neutral pH<sup>39,40</sup>;  
21 hence, we also analysed the products of CO<sub>2</sub>R with BN-GFLP in a 0.5 M NaHCO<sub>3</sub> saline electrolyte,  
22 instead of saturated CO<sub>2</sub> and confirmed the formation of the same C<sub>2+</sub> products (Supplementary Figs. 12,  
23 13, and 15). When combined, these results show that BN-GFLP is highly reactive toward HCO<sub>3</sub><sup>-</sup> and CO<sub>2</sub>  
24 reduction prior to the formation of CaCO<sub>3</sub>. In addition, the BN-GFLP cathode showed unprecedented and  
25 persistent catalytic performance for up to 100 h (Supplementary Fig. 17) without significant calcification

1 (Supplementary Fig. 18). This improved electrochemical stability might be related to  $\pi$ -electron donation  
2 from the graphitic framework.

### 3 **DFT calculations for mechanistic insights of BN-GFLP**

4 We used density functional theory (DFT) to elucidate the unique features of the BN-GFLP catalyst for  
5 CO<sub>2</sub>R and suggest a plausible C<sub>2+</sub> production mechanism (Fig. 4a). BN-GFLP was found to bind to CO<sub>2</sub>  
6 more strongly in a bidentate structure involving N–C and B–O than in a monodentate structure involving  
7 N–C, which agrees with the <sup>11</sup>B and <sup>15</sup>N MAS NMR studies (Fig. 2e,f). Furthermore, the bidentate  
8 structure favours the formation of the carbon monoxide (CO) intermediate from both CO<sub>2</sub> and HCO<sub>3</sub><sup>–</sup>,  
9 with a favourable Gibbs energy ( $\Delta G$ ) of -1.4 eV. Subsequently, direct C–C bond formation between the  
10 CO intermediate and another CO<sub>2</sub> results in the favourable formation of C<sub>2</sub>O<sub>3</sub> with a  $\Delta G$  of approximately  
11 -3.2 eV (Fig. 4a).

12 The observed unusual formation of C<sub>2</sub>O<sub>3</sub> can be explained by the sp<sup>2</sup>-type electronic structure of CO  
13 bonded to BN-GFLP, resulting in a single electron occupying the antibonding molecular orbital of CO  
14 (Supplementary Fig. 25), which increases the electron population on C and weakens the CO bond.  
15 Specifically, the triple bond of molecular CO induces a formal negative charge on C<sup>41</sup>. Furthermore, based  
16 on Bader charge analysis, the population of the C atom of CO bound to BN-GFLP is greater than that of  
17 a CO molecule by 0.28 electrons (Fig. 4b and Supplementary Fig. 26), which enhances C–C coupling  
18 between the negative C of the CO and positive C of a CO<sub>2</sub>, resulting in C<sub>2</sub>O<sub>3</sub> formation. Moreover,  
19 according to density of states (DOS) calculations, the antibonding state of the CO DOS in the -1 eV region  
20 is reduced through attachment to another CO<sub>2</sub> (Supplementary Fig. 25). This change in DOS makes CO<sub>2</sub>  
21 attachment favourable, which explains the marked decrease in Gibbs free energy when CO<sub>2</sub> bonds to CO.  
22 This thermodynamically favourable C<sub>2</sub>O<sub>3</sub> formation contributes to the activation of subsequent  
23 hydrogenation steps and selectivity towards C<sub>2+</sub> products. It is noteworthy that the present exothermic  
24 formation of C<sub>2</sub>O<sub>3</sub> by CO–CO<sub>2</sub> bonding is completely different from previously reported mechanisms  
25 that have endothermic CO–CO coupling steps for C<sub>2+</sub> production<sup>5,11,12,42–44</sup>. The exothermic formation of

1 C<sub>2</sub>O<sub>3</sub> is derived from the cooperative effects of the enhanced negative Bader charge on C and the  
2 antibonding dangling-bond electrons on the CO intermediate from the dual FLP binding sites on BN-  
3 GFLP, whereas the mono-binding B-GN and N-GN sites result in endothermically unfavourable C<sub>2</sub>O<sub>3</sub>  
4 formation. Furthermore, the dual binding mode on BN-GFLP highly stabilises the C–O bonds of  
5 H<sub>3</sub>CH<sub>2</sub>CO\* (ethanol intermediate) and H<sub>3</sub>CH<sub>2</sub>CH<sub>2</sub>CO\* (*n*-propanol intermediate), which leads to  
6 suppressed deoxygenation (Supplementary Fig. 27). Therefore, the BN-GFLP catalyst showed high  
7 alcohol selectivity in the C<sub>2+</sub> product distribution (Supplementary Fig. 15) over hydrocarbon products in  
8 the CO<sub>2</sub>R process<sup>45</sup> (Supplementary Fig. 27). Moreover, the energetic levels of all the species on BN-  
9 GFLP show favourable Gibbs free binding energies for conversion from CO<sub>2</sub> into C<sub>2+</sub> (ethanol and *n*-  
10 propanol). The potential-determining step for the overall reaction is the initial formation of CO (\*CO<sub>2</sub>H  
11 + H<sup>+</sup> + e<sup>-</sup> → \*CO + H<sub>2</sub>O), which was calculated to be uphill by 1.57 eV at *U* = 0 V. With an onset potential  
12 of -1.57 V<sub>RHE</sub> at pH 6.8, all proton–electron transfer steps have exothermic pathways. Thus, the DFT-  
13 calculated free energetics of CO<sub>2</sub>R on BN-GFLP rationalise the experimental results for C<sub>2+</sub> production  
14 from CO<sub>2</sub> in seawater.

## 15 **Conclusions**

16 In summary, we developed a CBS system to reduce CO<sub>2</sub> dissolved in seawater using a BN-GFLP catalytic  
17 cathode, resulting in the recovery of acidified seawater at a 87% FE. The unique features of BN-GFLP  
18 afford a novel dual CO<sub>2</sub> binding mode, which enables exothermic C–C coupling to deliver 95% selectivity  
19 for valuable multi-carbon products from CO<sub>2</sub>R. This state-of-the-art molecular design strategy for CO<sub>2</sub>R  
20 catalysts will contribute to saving the oceans and the atmosphere and to overcoming the current limitations  
21 of electrochemical catalytic performance in various fields.

22

23

# 1 **Methods**

2 **Materials.** N-methylpyrrolidone (NMP), pyrrole bis(pinacolato)diboron, CaCl<sub>2</sub>, TMP, <sup>15</sup>N urea were  
3 purchased from Sigma-Aldrich, USA, and used as received. Graphene nanopowder (multi-flakes) was  
4 obtained from Graphene Supermarket, USA. Other reagents and solvents were of analytical or high-  
5 performance liquid chromatography grade and used without further purification.

## 6 **Synthesis of heteroatom doped GN by sono-cavitation and nebulization synthesis (SNS).**

7 Preparation of precursor solutions: GN powders (15 mg) were added to NMP (30 mL) and dispersed by  
8 sonication for 2 hours with an ultrasonic probe (750 W, 20 kHz, Sonics and materials Inc., USA) to  
9 form a 0.5 mg mL<sup>-1</sup> spray solution. The solution was directly used to synthesize the N-GN with N<sub>2</sub> gas  
10 via SNS. To synthesize the both of B-GN and BN-GFLP, bis(pinacolato)diboron (30 mg) as boron  
11 dopant was added to the prepared GN solution (0.5 mg mL<sup>-1</sup>, 30 mL,) and sonicated for 1 hour.

12 Sono-cavitation and nebulization synthesis: The concurrently pumped spray coating was performed  
13 with an ExactaCoat system fixed with an impact ultrasonic nozzle (Sono-Tek Co.). The prepared  
14 precursor solutions were sequentially fed into the ultrasonic nozzle (180 kHz) system at the spray rate  
15 of 0.3 mL min<sup>-1</sup>. The nozzle-to-substrate distance (10 cm) and the compressed N<sub>2</sub> or Ar gas pressure  
16 (3.0 psi) were used to spray the gas diffusion layer substrate (carbon felt, area: 5 cm × 5 cm, thickness:  
17 ~4.1 mm) at a spray speed of 20 mm s<sup>-1</sup> on a temperature-controlled (150 °C) stage. The resulting  
18 products were cool to room temperature and washed with water, ethanol, and acetone to remove the  
19 unreacted precursor and impurities. The residual solvent was evaporated in a vacuum oven at 200 °C for  
20 24 hours. As a result, the SNS process with GN solution synthesized the GN (with Ar gas carrier) and  
21 the N-GN (with N<sub>2</sub> gas carrier) catalytic cathodes. The SNS process with boron dopant mixed GN  
22 solution synthesized the B-GN (with Ar gas carrier) and the BN-GFLP (with N<sub>2</sub> gas carrier) catalytic  
23 cathodes.  
24

1 **Surface chemistry analysis.** The structure and doping of the carbon materials treated by the SNS were  
2 analyzed using high-resolution transmission electron microscopy (TEM, JEOL JEM-2100F (Cs),  
3 operating at 200 kV), Raman spectroscopy (Alpha 300R, WITec GmbH), X-ray photoelectron  
4 spectroscopy (Thermo Fisher, K-alpha), and energy dispersive spectroscopy (resolution: 128 eV,  
5 Oxford, x-Max T-80). Raman spectra and images for the samples were obtained with a micro-Raman  
6 system with a 532 nm laser. In order to avoid the laser-induced thermal effects or damage to the  
7 samples, the incident laser power was controlled to below 4 mW.

8  
9 **Nuclear magnetic resonance (NMR) spectroscopy.** All the NMR experiments were performed on a  
10 Varian VNMRS 600 MHz spectrometer at resonance frequencies of 599.83, 242.82, 192.45, and 60.79  
11 MHz for  $^1\text{H}$ ,  $^{31}\text{P}$ ,  $^{11}\text{B}$ , and  $^{15}\text{N}$  nucleus, respectively. The NMR spectra were recorded using a 1.6 mm  
12 HXY fast MAS triple resonance probe and a spinning rate of 35, 25, and 20 kHz. A  $\pi/2$  pulse lengths of  
13 1.33, 1.55, 4.80, and 2.70  $\mu\text{s}$ , and a recycle delay of 5, 3, 3, and 200 s were used for the  $^1\text{H}$ ,  $^{31}\text{P}$ ,  $^{11}\text{B}$ , and  
14  $^{15}\text{N}$  MAS NMR experiments, respectively. The chemical shifts of  $^1\text{H}$ ,  $^{31}\text{P}$ ,  $^{11}\text{B}$ , and  $^{15}\text{N}$  were externally  
15 referenced to hexamethylbenzene, 1 M  $\text{H}_3\text{PO}_4$  in  $\text{D}_2\text{O}$ , 15%  $\text{BF}_3 \cdot \text{O}(\text{C}_2\text{H}_5)_2$  in  $\text{CDCl}_3$ , and  $^{15}\text{N}$  labeled  
16 glycine, respectively.

17 **Lewis acidity and Lewis basicity:** Prior to the adsorption of probe molecules, the samples were placed  
18 in glass tubes and then connected to a vacuum line for dehydration. The temperature was gradually  
19 increased at a rate of 1 K/min, and the samples were kept at a final temperature of 453 K at a pressure  
20 below  $10^{-3}$  Pa over a period of 10 hours and then cooled. After the samples cooled down to the room  
21 temperature, sufficient pyrrole molecules were introduced into the activated samples and then frozen by  
22 liquid  $\text{N}_2$ . Subsequently, the samples were evacuated at 333 K for 2 hours on the vacuum line to  
23 eliminate physisorbed pyrrole molecules after the adsorption was equilibrated. Finally, the sample tubes  
24 were flame-sealed. The similar approaches were also employed in the preparation of trimethylphosphine

1 (TMP) adsorbed samples. Prior to NMR experiments, the sealed sample was transferred into a ZrO<sub>2</sub>  
2 rotor with a Kel-F end-cap under a dry nitrogen atmosphere in a glovebox.

3 B–O and N–C interaction between BN-GFLP and CO<sub>2</sub>: <sup>11</sup>B NMR and <sup>15</sup>N NMR spectra of graphitic  
4 frustrated Lewis pair (GFLP, BN-GFLP) before and after external gas stimuli were tested by VRMS  
5 600 MHz of Varian Instrument. For the synthesis of <sup>15</sup>N labeled BN-GFLP, <sup>15</sup>N urea was used as N  
6 dopant, and Ar carrier gas was used in SNS process. Into 60 mL vial were added GN precursor (15 mg),  
7 bis(pinacolato)diboron (30 mg), <sup>15</sup>N urea (30 mg), and 30 mL of N-methyl-2-pyrrolidone. The prepared  
8 precursor solution was fed into the ultrasonic nozzle (180 kHz) at the 0.3 mL/min of flow rate through  
9 syringe pump. The ultrasonic nozzle-to-substrate distance (10 cm) and the compressed Ar gas pressure  
10 (3.0 psi) were used to spray deposition to the substrate (SUS plate) on a temperature-controlled (150 °C)  
11 heating stage. The resulting products were washed and the residual solvent was evaporated with same  
12 procedure of SNS method. Furthermore, to quantitatively control the CO<sub>2</sub> aeration amount to a given  
13 BN-GFLP sample, we used a microflow-pump GHN-1 (CHIYODA SEIKI Co.) connected into a gas  
14 cylinder (10 L), and the gas flow rate was fixed at 50.0 mL s<sup>-1</sup> and the gas pressure was constant at 1.0  
15 bar.

16

17 **Electron paramagnetic resonance (EPR) spectroscopy.** The X-band continuous wave electron  
18 paramagnetic resonance spectroscopy signals were collected by EMX plus 6/1 spectrometer (Bruker  
19 BioSpin, MA, USA). The radical defects of heteroatom doped graphene nanopowders were recorded by  
20 X-band CW-EPR (Bruker EMX plus 6/1 spectrometer equipped with Oxford Instrument ESR900 liquid  
21 He cryostat using an Oxford ITC 503 temperature controller). These analyses were progressed at  
22 Western Seoul Center, Korea Basic Science Institute (KBSi).

23

24 **Temperature programmed desorption (TPD).** TPD measurements were made on the AutoChem 1  
25 2920 instrument. For CO<sub>2</sub>-TPD measurement, 200 mg of catalyst powder was put into quartz tube and

1 adsorption of CO<sub>2</sub> was performed in 10%CO<sub>2</sub>/He gas flow for 3 h at 50 °C. After 0.5 hours of purging  
2 with He (99.999%) gas to remove residual CO<sub>2</sub>, it was heated from 50 °C to 400 °C at a rate of 10 °C  
3 min<sup>-1</sup>. The TPD signal was recorded using a thermal conductivity detector.

4  
5 **CO<sub>2</sub> reduction battery in seawater (CBS) system components preparation.** Coin-type CBS system  
6 consists of Na-metal anode with aprotic electrolyte (1 M sodium trifluoromethanesulfonate (NaCF<sub>3</sub>SO<sub>3</sub>))  
7 in tetraethylene glycol dimethyl ether (TEGDME)), carbon felt-support current collector with seawater  
8 cathode, and the Na super ion conductor (NASICON) separate. The carbon felt substrate (XP-30A,  
9 Toyobo Co., Ltd) was heat-treated at 500 °C in ambient atmosphere for 4 hours with the ramping ratio  
10 of 5 °C min<sup>-1</sup> to enhance the hydrophilicity, before the aforementioned SNS process. The thickness of  
11 heat-treated carbon felt is ~4.1 mm. Natural seawater was collected from the Ilsan beach, Ulsan,  
12 Republic of Korea (GPS: 35.497005, 129.430996). NASICON ceramic solid electrolyte (Na<sub>1+x</sub>Zr<sub>2</sub>Si<sub>x</sub>P<sub>3-x</sub>  
13 O<sub>12</sub>, x=2) was purchased from 4TOONE Energy Co., Ltd<sup>17</sup>. All chemicals are purchased from Sigma  
14 Aldrich and used without any purification.

15  
16 **Electrochemistry.** All electrochemical evaluations of CBS system were performed by using a battery  
17 measurement system (VMP3 Multichannel Workstation, BioLogic). For the CO<sub>2</sub> reduction  
18 electrocatalytic activity, the 2-electrode gas-tight Swagelok type CBS system (Extended Data Fig. 3)  
19 was connected to linear sweep voltammetry (LSV) and lab-built pressure monitoring system. The  
20 hydrogen evolution of GFLP was measured by using lab-built in situ differential electrochemical mass  
21 spectroscopy (DEMS). The details of DEMS systems are described elsewhere<sup>46</sup>. The LED panel was  
22 prepared by connecting the 36 LED (5 mm, green color) onto the Arduino Breadboard (MB-102) in  
23 parallel. To monitoring the pH (Five Easy FE20, Mettler Toledo) of seawater, the flowable zig type  
24 CBS system (4TOONE Energy Co., Ltd) was placed into the plastic container. The pH of seawater was  
25 controlled by bubbling the CO<sub>2</sub> gas before discharge.

1  
2  
3  
4  
5  
6  
7  
8  
9  
10  
11  
12  
13  
14  
15  
16  
17  
18  
19  
20  
21  
22  
23  
24

**Product analysis.** Quantitative analysis of the liquid products formed during electrolysis was performed with high performance liquid chromatography (HPLC). After electrolysis, aliquots of the catholyte were collected and analyzed with HPLC (Agilent, 1200 series). Sample vials were placed in a chilled autosampler and 10  $\mu$ L of each sample was injected onto the column. Synergi Polar C18 column (4  $\mu$ m, 150  $\times$  4.6 mm) placed in series were used to obtain satisfactory product separation. During analysis the column oven was maintained at a steady temperature of 25  $^{\circ}$ C, with a steady flow rate of 0.800 mL/min of 100% H<sub>2</sub>O (isocratic) as eluent. The effluent stream coming from the column was passed through a refractive index detector (RID) for product detection. Standard calibrations were performed using dilute solutions of the expected products, methanol, ethanol, n-propanol, and formic acid. Reported Faradaic efficiencies were averaged from at least three different electrolysis experiments. Electrospray ionization mass spectroscopy (ESI-MS) was carried out on a AccuTOF 4G+ DART (JEOL) for confirming the molecular weight of all the samples. Samples containing 10-100  $\mu$ g of an analyte were introduced using direct injection to mass spectrometer with a flow rate of 3  $\mu$ l/min. The potential between the spray needle and the orifice was set to 2.0 kV. The detector potential was 2.5 kV. The AccuTOF 4G+ DART instrument equipped with an ESI source with ion funnel, was operated in the positive or negative ion mode and calibrated before each analysis with the Tunemix mixture (Agilent) by a quadratic method.

**Evaluation of CO<sub>2</sub>R performance.** For liquid products, the following method was used for the calculation of Faradaic efficiency. The concentration of species *l* ( $c_l$  (mol L<sup>-1</sup>)) was calculated from the HPLC with internal standard method. With  $z_l$ , Faraday constant and the electrolyte volume ( $V$  (L)), the partial charge to produce species *l* ( $q_l$  (C)) was calculated. The Faradaic efficiency for species *l* (FE<sub>*l*</sub>) is the percentage of the partial charge in the total charge passed ( $q_{tot}$  (C)):

$$FE_l = \frac{q_l}{q_{tot}} = \frac{96485 \times c_l \times V \times z_l}{q_{tot}} \times 100\%$$

Formation rate (R) for each species and C<sub>2+</sub> selectivity were calculated using the following equations:

$$R_l = \frac{q_{tot} \times FE_l}{96485 \times z_l \times t \times S} = \frac{c_l \times V}{t \times S}$$

where t was the electrolysis time (h) and S was the geometric area of the electrode (cm<sup>2</sup>).

$$C_{2+} \text{ selectivity (\%)} = \frac{2R_{ethanol} + 3R_{Propanol}}{R_{methanol} + 2R_{ethanol} + 3R_{Propanol}} \times 100\%$$

**DFT calculation method.** Spin-polarized Density Functional Theory calculations were performed by using Vienna Ab-initio Simulation Package (VASP) code<sup>47</sup>. The plane wave cutoff energy of 400 eV was employed with PBE parameterization of GGA exchange-correlation functional<sup>48</sup>. We adopted the ribbon structure model with the lattice parameter  $a = 17.04 \text{ \AA}$ ,  $b = 25.00 \text{ \AA}$ ,  $c = 20.00 \text{ \AA}$ , where the ribbon is extended along the a-direction and sufficient vacuum regions greater than 15 Å are inserted along the other directions to minimize the unphysical interaction between periodic images. All structures were fully optimized in the 1x1x1 k-mesh until the force is less than 0.01 eV/Å with van der Waals correction by Grimme's scheme, D3 method<sup>49</sup>. In HCO<sub>3</sub><sup>-</sup> calculation, we constructed cell with different length, and extrapolated their energy to get appropriate binding energy without unphysical interactions in periodic boundary condition. For density of states (DOS) calculation, 8x1x1 k-mesh was used. We calculated the Gibbs free energy by the equation,  $\Delta G = \Delta E^{DFT} + \Delta ZPE - T\Delta S + \Delta G_U + \Delta G_{pH}$ <sup>50</sup>.  $\Delta E^{DFT}$  refers to the calculated adsorption energy difference between subsequent intermediates proposed by Norskov et al.<sup>51</sup>. Zero-point energy and vibrational entropy,  $\Delta ZPE$  and  $T\Delta S$ , were calculated by vibrational frequencies of each intermediates. Under the applied electrode potential  $U$ ,  $\Delta G_U = -eU$  correction was added to the total Gibbs free energy.  $\Delta G_{pH}$  denotes correction of solution acidity by  $-k_B T \ln[H^+]$ . We performed the Bader charge analysis for CO and C<sub>2</sub>O<sub>3</sub> structure to figure out the effect of electrostatic interaction between adsorbed CO and CO<sub>2</sub> molecule to form C<sub>2+</sub> product<sup>52</sup>.

1

## 2 **Data availability**

3 The authors declare that all data supporting the findings of this study are available in the paper and  
4 Supplementary Information. Additional datasets related to this study are available from the corresponding  
5 authors on reasonable request.

6

# 1 Reference

- 2 1. Pandolfi, J. M., Connolly, S. R., Marshall, D. J. & Cohen, A. L. Projecting coral reef futures under global warming  
3 and ocean acidification. *Science* **333**, 418-422 (2011).
- 4 2. Hoegh-Guldberg, O. et al. Coral reefs under rapid climate change and ocean acidification. *Science* **318**, 1737-1742  
5 (2007).
- 6 3. Liu, Y. W., Sutton, J., Ries, J. B. & Eagle, R. A. Eagle, Regulation of calcification site pH is a polyphyletic but not  
7 always governing response to ocean acidification. *Sci. Adv.* **6**, eaax1314 (2020).
- 8 4. Foster, T., Falter, J. L., McCulloch, M. T. & Clode, P. L. Ocean acidification causes structural deformities in juvenile  
9 coral skeletons. *Sci. Adv.* **2**, e1501130 (2016).
- 10 5. Nitopi, S. et al. Progress and perspectives of electrochemical CO<sub>2</sub> reduction on copper in aqueous electrolyte. *Chem.*  
11 *Rev.* **119**, 7610–7672 (2019).
- 12 6. Mariano, R. G., McKelvey, K., White, H. S. & Kanan, M. W. Selective increase in CO<sub>2</sub> electroreduction activity at  
13 grain-boundary surface terminations. *Science* **358**, 1187-1192 (2017).
- 14 7. Gao, S. et al. Partially oxidized atomic cobalt layers for carbon dioxide electroreduction to liquid fuel. *Nature* **529**,  
15 68-71 (2016).
- 16 8. Gao, D. et al. Enhancing CO<sub>2</sub> Electroreduction with the metal-oxide interface. *J. Am. Chem. Soc.* **139**, 5652-5655  
17 (2017).
- 18 9. Lin, S. et al. Covalent organic frameworks comprising cobalt porphyrins for catalytic CO<sub>2</sub> reduction in water. *Science*  
19 **349**, 1208-1213 (2015).
- 20 10. Kornienko, N. et al. Metal-organic frameworks for electrocatalytic reduction of carbon dioxide. *J. Am. Chem. Soc.*  
21 **137**, 14129-14135 (2015).
- 22 11. Gao, D., Arán-Ais, R. M., Jeon, H. S. & Roldan Cuenya, B. Rational catalyst and electrolyte design for CO<sub>2</sub>  
23 electroreduction towards multicarbon products. *Nat. Catal.* **2**, 198-210 (2019).
- 24 12. Wang, H. et al. Synergistic enhancement of electrocatalytic CO<sub>2</sub> reduction to C<sub>2</sub> oxygenates at nitrogen-doped  
25 nanodiamonds/Cu interface. *Nat. Nanotechnol.* **15**, 131-137 (2020).
- 26 13. Dinh, C. T. et al. Quintero-Bermudez, Y. J. Pang, D. Sinton, E. H. Sargent, CO<sub>2</sub> electroreduction to ethylene via  
27 hydroxide-mediated copper catalysis at an abrupt interface. *Science* **360**, 783-787 (2018).
- 28 14. Lee, C.-Y. & Wallace, G. G. CO<sub>2</sub> electrolysis in seawater: calcification effect and a hybrid self-powered concept. *J.*  
29 *Mater. Chem. A* **6**, 23301-23307 (2018).
- 30 15. Gabrielli, C., Jaouhari, R., Joiret, S., Maurin, G. & Rousseau, P. Study of the electrochemical deposition of CaCO<sub>3</sub>  
31 by in situ Raman spectroscopy. *J. Electrochem. Soc.* **150**, C478-C484 (2003).
- 32 16. Nakata, K., Ozaki, T., Terashima, C., Fujishima, A. & Einaga, Y. High-yield electrochemical production of  
33 formaldehyde from CO<sub>2</sub> and seawater. *Angew. Chem. Int. Ed.* **53**, 871-874 (2014).
- 34 17. Hwang, S. M. et al. Rechargeable seawater batteries—from concept to applications. *Adv. Mater.* **31**, 1804936 (2019).
- 35 18. Kim, D. H. et al. Reliable seawater battery anode: controlled sodium nucleation via deactivation of the current  
36 collector surface. *J. Mater. Chem. A* **6**, 19672-19680 (2018).
- 37 19. Stephan, D. W. The broadening reach of frustrated Lewis pair chemistry. *Science* **354**, aaf7229 (2016).
- 38 20. Chen, L., Liu, R., Hao, X. & Yan, Q. CO<sub>2</sub>-cross-linked frustrated Lewis networks as gas-regulated dynamic covalent  
39 materials. *Angew. Chem. Int. Ed.* **58**, 264-268 (2019).
- 40 21. Momming, C. M. et al. Reversible metal-free carbon dioxide binding by frustrated Lewis pairs. *Angew. Chem. Int.*  
41 *Ed.* **48**, 6643-6646 (2009).
- 42 22. Courtemanche, M. A., Legare, M. A., Maron, L. & Fontaine, F. G. Reducing CO<sub>2</sub> to methanol using frustrated Lewis  
43 pairs: on the mechanism of phosphine-borane-mediated hydroboration of CO<sub>2</sub>. *J. Am. Chem. Soc.* **136**, 10708-10717  
44 (2014).
- 45 23. Ding, Y. et al. Heterogeneous metal-free catalyst for hydrogenation: Lewis acid-base pairs integrated into a carbon  
46 lattice. *Angew. Chem. Int. Ed.* **57**, 13800-13804 (2018).
- 47 24. Kim, H. T. et al. Carbon-heteroatom bond formation by an ultrasonic chemical reaction for energy storage systems.  
48 *Adv. Mater.* **29**, 1702747 (2017).
- 49 25. Bang, J. H. & Suslick, K. S. Applications of ultrasound to the synthesis of nanostructured materials. *Adv. Mater.* **22**,  
50 1039-1059 (2010).

- 1 26. Suslick, K. S. Sonochemistry. *Science* **247**, 1439-1445 (1990).
- 2 27. Xu, H. & Suslick, K. S. Sonochemical preparation of functionalized graphenes. *J. Am. Chem. Soc.* **133**, 9148-9151  
3 (2011).
- 4 28. Tampieri, F., Silvestrini, S., Riccò, R., Maggini, M. & Barbon, A. A comparative electron paramagnetic resonance  
5 study of expanded graphites and graphene. *J. Mater. Chem. C* **2**, 8105-8112 (2014).
- 6 29. Panich, A. M. et al. Structure and magnetic properties of pristine and Fe-doped micro- and nanographenes. *J. Phys.*  
7 *Chem. C* **120**, 3042-3053 (2016).
- 8 30. Zheng, A., Liu, S. B. & Deng, F. <sup>31</sup>P NMR chemical shifts of phosphorus probes as reliable and practical acidity  
9 scales for solid and liquid catalysts. *Chem. Rev.* **117**, 12475-12531 (2017).
- 10 31. Wiper, P. V., Amelse, J. & Mafra, L. Multinuclear solid-state NMR characterization of the Brønsted/Lewis acid  
11 properties in the BP HAMS-1B (H-[B]-ZSM-5) borosilicate molecular sieve using adsorbed TMPO and TBPO probe  
12 molecules. *J. Catal.* **316**, 240-250 (2014).
- 13 32. Chu, Y. et al. Acidic strengths of Brønsted and Lewis acid sites in solid acids scaled by <sup>31</sup>P NMR chemical shifts of  
14 adsorbed trimethylphosphine. *J. Phys. Chem. C* **115**, 7660-7667 (2011).
- 15 33. Yi, X. et al. An NMR scale for measuring the base strength of solid catalysts with pyrrole probe: A combined solid-  
16 state NMR experiment and theoretical calculation study. *J. Phys. Chem. C* **121**, 3887-3895 (2017).
- 17 34. Sánchez-Sánchez, M. & Blasco, T. Pyrrole as an NMR probe molecule to characterise zeolite basicity. *Chem.*  
18 *Commun.* **6**, 491-492 (2000).
- 19 35. Han, J. et al. Development of coin-type cell and engineering of its compartments for rechargeable seawater batteries.  
20 *J. Power Sources* **374**, 24-30 (2018).
- 21 36. Lim, C. H., Holder, A. M., Hynes, J. T. & Musgrave, C. B. Roles of the Lewis acid and base in the chemical reduction  
22 of CO<sub>2</sub> catalyzed by frustrated Lewis pairs. *Inorg. Chem.* **52**, 10062-10066 (2013).
- 23 37. Webb, G. A. Annual reports on NMR spectroscopy preface. *Annu. Rep. NMR Spectro.* **91**, Ix-Ix (2017).
- 24 38. Mastikhin, V. M., Mudrakovsky, I. L. & Filimonova, S. V. Probing the Lewis acidity of heterogeneous catalysts by  
25 N-15 NMR of adsorbed N<sub>2</sub>O. *Chem. Phys. Lett.* **149**, 175-179 (1988).
- 26 39. Andersen, C. B. Understanding carbonate equilibria by measuring alkalinity in experimental and natural systems. *J.*  
27 *Geosci. Educ.* **50**, 389-403 (2018).
- 28 40. Roldan, A. et al. Bio-inspired CO<sub>2</sub> conversion by iron sulfide catalysts under sustainable conditions. *Chem. Commun.*  
29 **51**, 7501-7504 (2015).
- 30 41. Kim, H. et al. Intriguing electrostatic potential of CO: Negative bond-ends and positive bond-cylindrical-surface. *Sci.*  
31 *Rep.* **5**, 16307 (2015).
- 32 42. Liu, C. et al. Stability and effects of subsurface oxygen in oxide-derived Cu catalyst for CO<sub>2</sub> reduction. *J. Phys. Chem.*  
33 *C* **121**, 25010-25017 (2017).
- 34 43. Calle-Vallejo, F. & Koper, M. T. Theoretical considerations on the electroreduction of CO to C<sub>2</sub> species on Cu(100)  
35 electrodes. *Angew. Chem. Int. Ed.* **52**, 7282-7285 (2013).
- 36 44. Rahaman, M., Dutta, A., Zanetti, A. & Broekmann, P. Electrochemical reduction of CO<sub>2</sub> into multicarbon Alcohols  
37 on activated Cu mesh catalysts: An identical location (IL) Study. *ACS Catal.* **7**, 7946-7956 (2017).
- 38 45. Wang, X. et al. Efficient electrically powered CO<sub>2</sub>-to-ethanol via suppression of deoxygenation. *Nat. Energy* **5**, 478-  
39 486 (2020).
- 40 46. McCloskey, B. D., Bethune, D. S., Shelby, R. M., Girishkumar, G. & Luntz, A. C. Solvents' critical role in nonaqueous  
41 lithium-oxygen battery electrochemistry. *J. Phys. Chem. Lett.* **2**, 1161-1166 (2011).
- 42 47. Kresse, G. & Furthmüller, J. Efficiency of ab-initio total energy calculations for metals and semiconductors using a  
43 plane-wave basis set. *Comput. Mater. Sci.*, **6**, 15-50 (1996).
- 44 48. Perdew, J. P., Burke, K. & Enzerhof, M. Generalized gradient approximation made simple. *Phys. Rev. Lett.*, **77**,  
45 3865 (1996).
- 46 49. Bučko, T., Lebègue, S., Hafner, J. & Ángyán, J. G. Tkatchenko-Scheffler van der Waals correction method with and  
47 without self-consistent screening applied to solids. *Phys. Rev. B*, **87**, 064110 (2013).
- 48 50. Norskov, J. K. et al. Origin of the overpotential for oxygen reduction at a fuel-cell cathode. *J. Phys. Chem. B*, **108**,  
49 17886-17892 (2004).
- 50 51. Tang, W., Sanville, E. & Henkelman, G. A grid-based Bader analysis algorithm without lattice bias. *J. Phys. Condens.*  
51 *Matter*, **21**, 084204 (2009).
- 52 52. Man, I. C. et al. Universality in oxygen evolution electrocatalysis on oxide surfaces. *ChemCatChem*, **3**, 1159-1165  
53 (2011).

## 1 **Acknowledgements**

2 This work was supported by the National Research Foundation of Korea (NRF-2016M1A2A2940910,  
3 2017M1A2A2087813, 2017M3A7B4052802, 2019R1A2C2007311 and 2018R1D1A1B07045983), the  
4 Korea Institute of Energy Technology Evaluation and Planning (20183010013900), and the 2020 UNIST  
5 Research Fund (1.190004.01). Computational work was supported by KISTI (KSC-2019-CRE-0221) and  
6 the UNIST Supercomputing Center.

## 7 **Author contribution**

8 T.-H.K., S.J.K., and G.L. supervised this project. H.-T.K. and J.P. designed and carried out all of the  
9 experiments. J.M. carried out the DFT calculation. H.-T.K., J.K., and S.K. performed the catalyst  
10 preparation, characterization, and optimization of SNS method. H.-T.K. carried out XPS, EPR, and MAS  
11 NMR, and Raman spectroscopy analyses. J.P. carried out home-built DEMS set-up, device fabrication,  
12 characterization, and all of the electrochemical analysis. H.-T.K., H.S., and D.-H.R. participated in ESI-  
13 MS, HPLC analyses and HR-TEM imaging. All authors discussed the results and assisted during  
14 manuscript preparation.

## 15 **Competing financial interests**

16 The authors declare no competing financial interest.

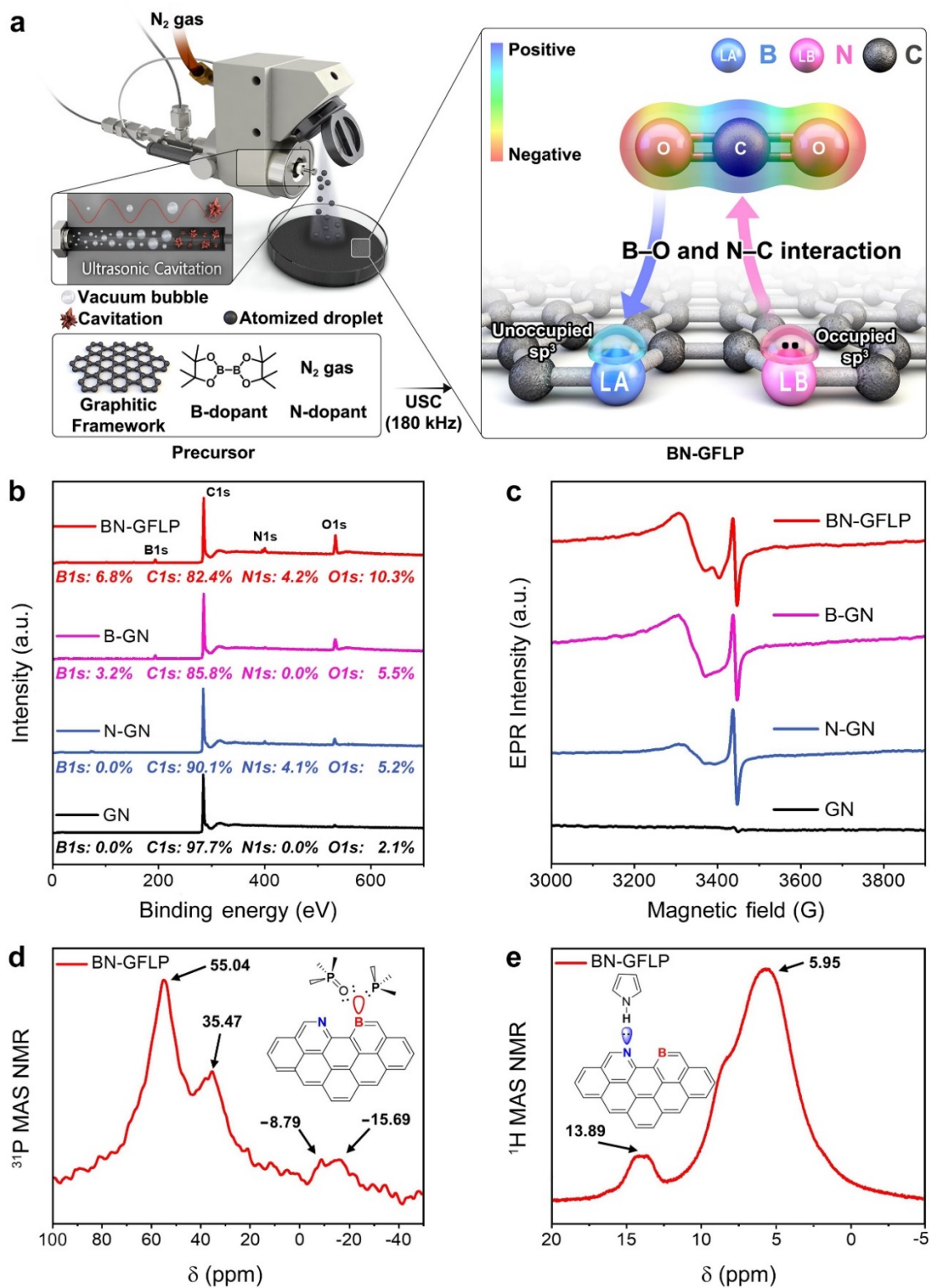
## 17 **Additional information**

18 **Supplementary information** is available for this paper at

19 **Reprints and permissions information** is available at [www.nature.com/reprints](http://www.nature.com/reprints).

20 **Correspondence and requests for materials** should be addressed to T.-H.K.

21 **Publisher's note:** Springer Nature remains neutral with regard to jurisdictional claims in published



1

2 **Fig. 1: Sono-cavitation and nebulisation synthesis (SNS) process and BN-GFLP structure characterisation. (a)**  
 3 Schematic of the SNS process for BN-GFLP synthesis and molecular interactions between BN-GFLP and CO<sub>2</sub>. **(b)** Survey  
 4 XPS spectra (normalised to C<sub>1s</sub>) and **(c)** EPR spectra of GN, N-GN, B-GN, and BN-GFLP at 10 K. **(d)** <sup>31</sup>P MAS NMR  
 5 spectrum of TMP on BN-GFLP. **(e)** <sup>1</sup>H MAS NMR spectrum of pyrrole adsorbed on BN-GFLP.

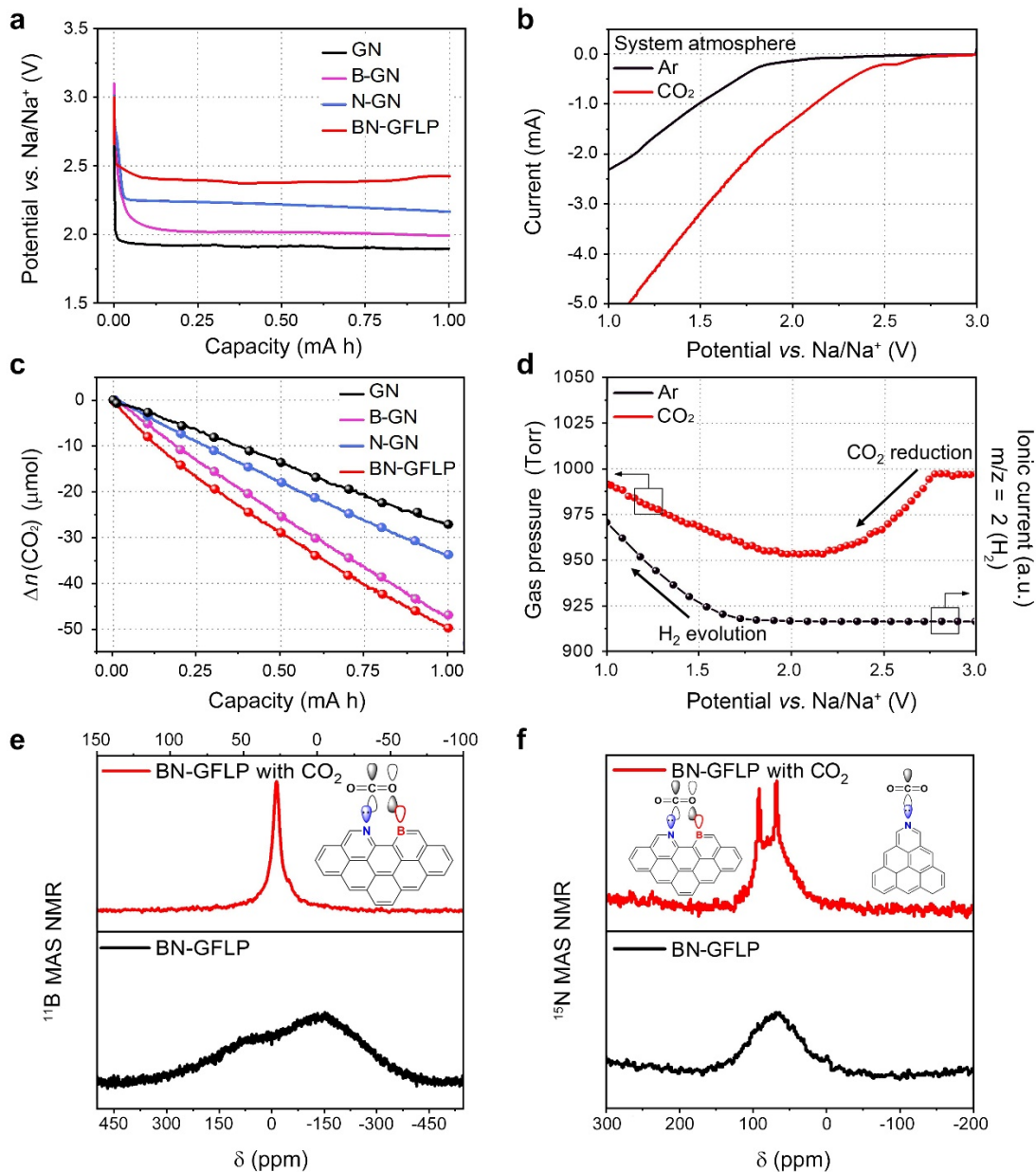


**Fig. 2: Electrochemical CO<sub>2</sub> reduction on the BN-GFLP electrode in seawater.** (a) Galvanostatic discharge voltage profiles of the CBS system with the prepared catalysts at a fixed current density of 0.13 mA cm<sup>-2</sup> and (b) LSV profiles of the BN-GFLP catalyst under various system atmospheres in the 3.0–1.0 V voltage window at a sweep rate of 0.1 mV s<sup>-1</sup>. (c) Quantitative CO<sub>2</sub> gas consumption during the galvanostatic discharge process in (a). (d) Inner pressure decay (red) and complementary DEMS (black) results corresponding to the LSV profiles in (b). (e) <sup>11</sup>B and (f) <sup>15</sup>N MAS NMR spectra of BN-GFLP with (red) and without (black) CO<sub>2</sub> stimulus. Possible binding configurations between BN-GFLP and CO<sub>2</sub> are shown in the insets of (e) and (f).

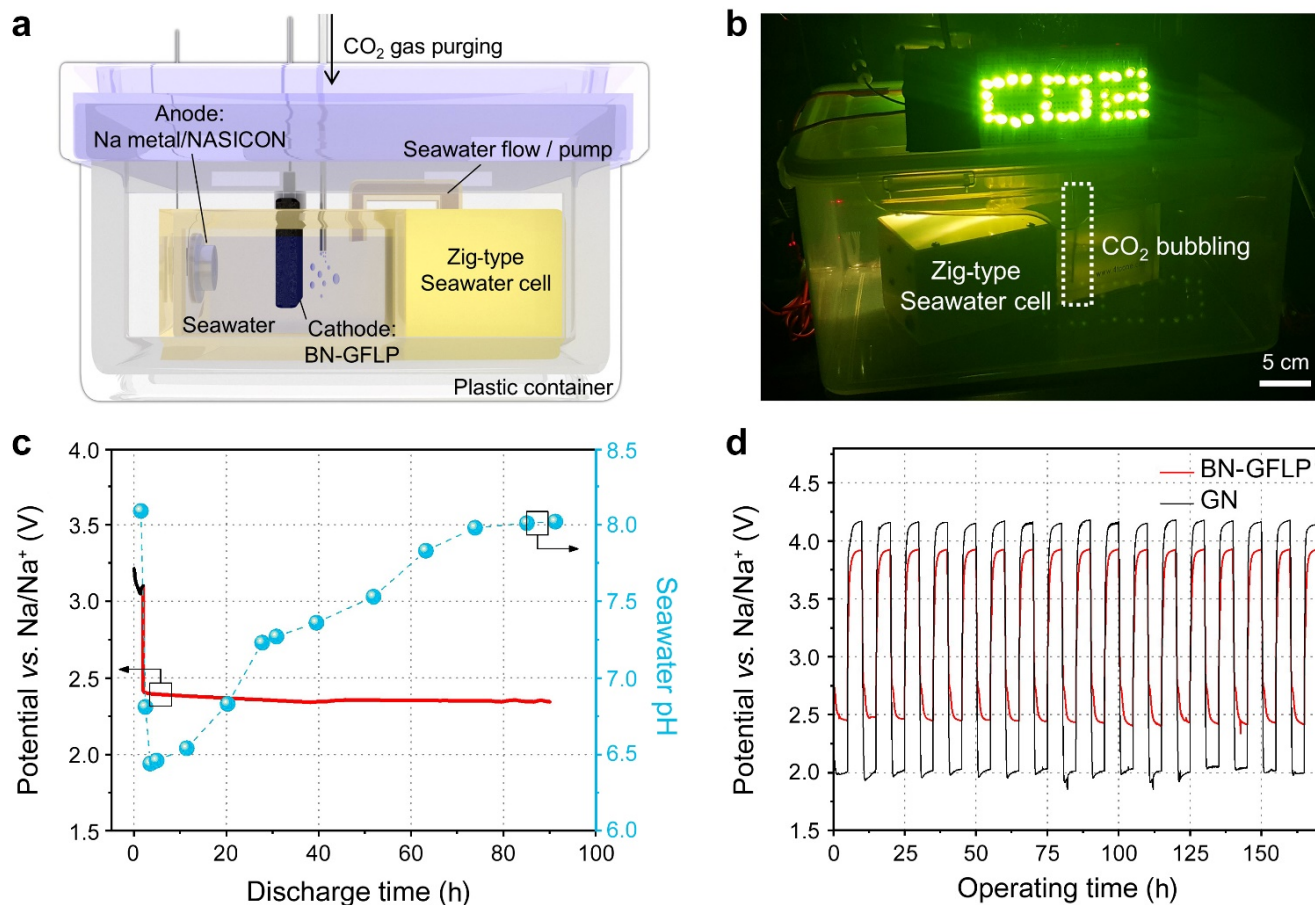


**Fig. 3: Electric energy harvesting and stability of the CBS system with the BN-GFLP cathode during CO<sub>2</sub>R. (a)**

Schematic of the zig-type CBS system. **(b)** Digital photograph of 36 LEDs powered by the CBS system. **(c)** Seawater pH as a function of time during CO<sub>2</sub>R with a fixed current density of 0.13 mA cm<sup>-2</sup>. The pH was controlled by bubbling CO<sub>2</sub> into the seawater. **(d)** Galvanostatic charge-discharge voltage plots of zig-type CBS cells with BN-GFLP and control GN cathodes.

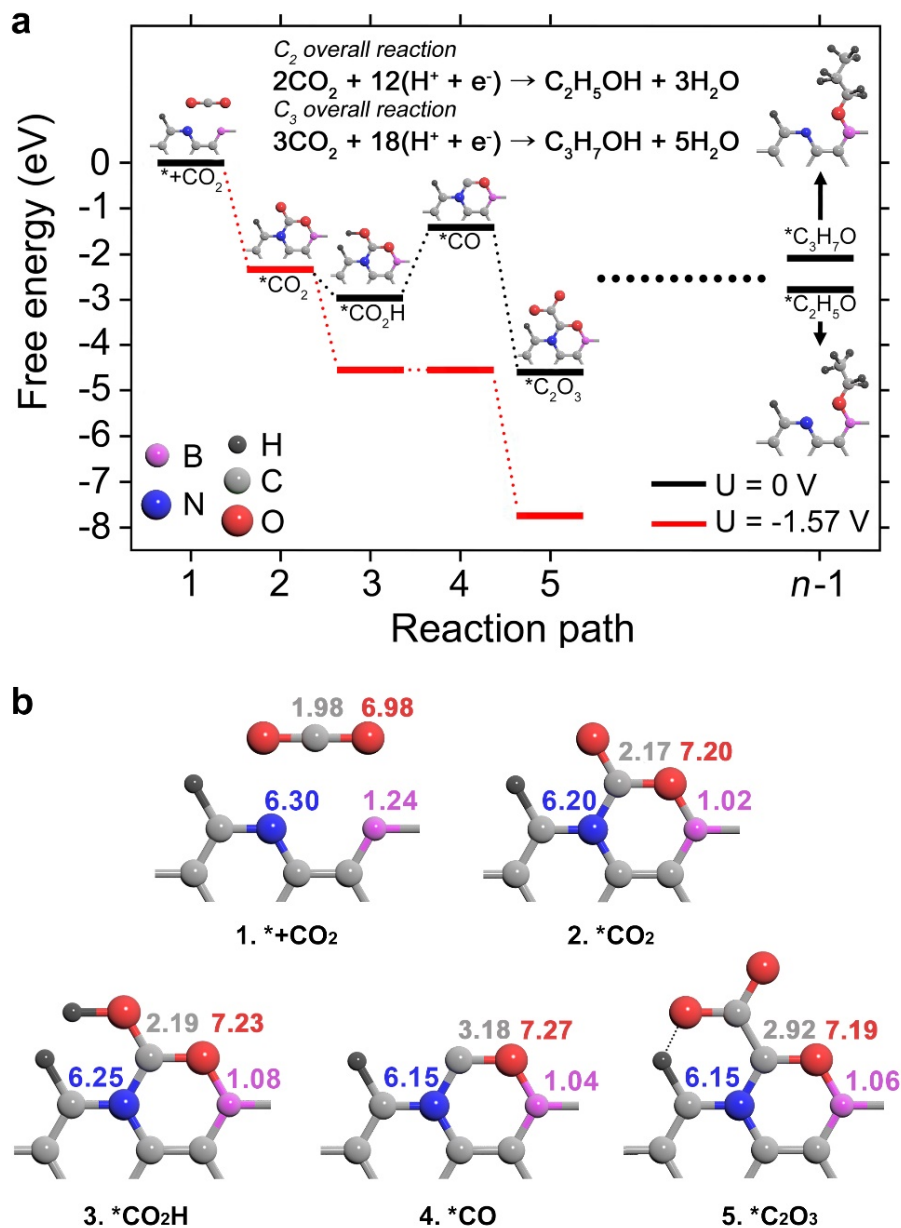


**Fig. 4:** DFT calculations of the BN-GFLP catalyst for  $\text{CO}_2\text{R}$ . (a) Gibbs free energy diagram for  $\text{CO}_2\text{R}$  reaction to  $\text{C}_{2+}$  products on the BN-GFLP electrode. The red lines show the optimal mechanism for  $\text{C}_{2+}$  product formation at an applied potential of -1.57 V. According to the reaction path at 0 V applied potential (black lines)  $\text{CO}-\text{CO}_2$  coupling ( $4 \rightarrow 5$ ) is highly favourable, with a Gibbs free energy difference of -3.2 eV. (b) Bader charges ( $e^-$ ) of the active sites in BN-GFLP and the reaction-path intermediates corresponding to (a). The Bader charge of each atom is shown in the same color as the corresponding atom: hydrogen (black), nitrogen (blue), boron (purple), carbon (grey), and oxygen (red).

# Figures

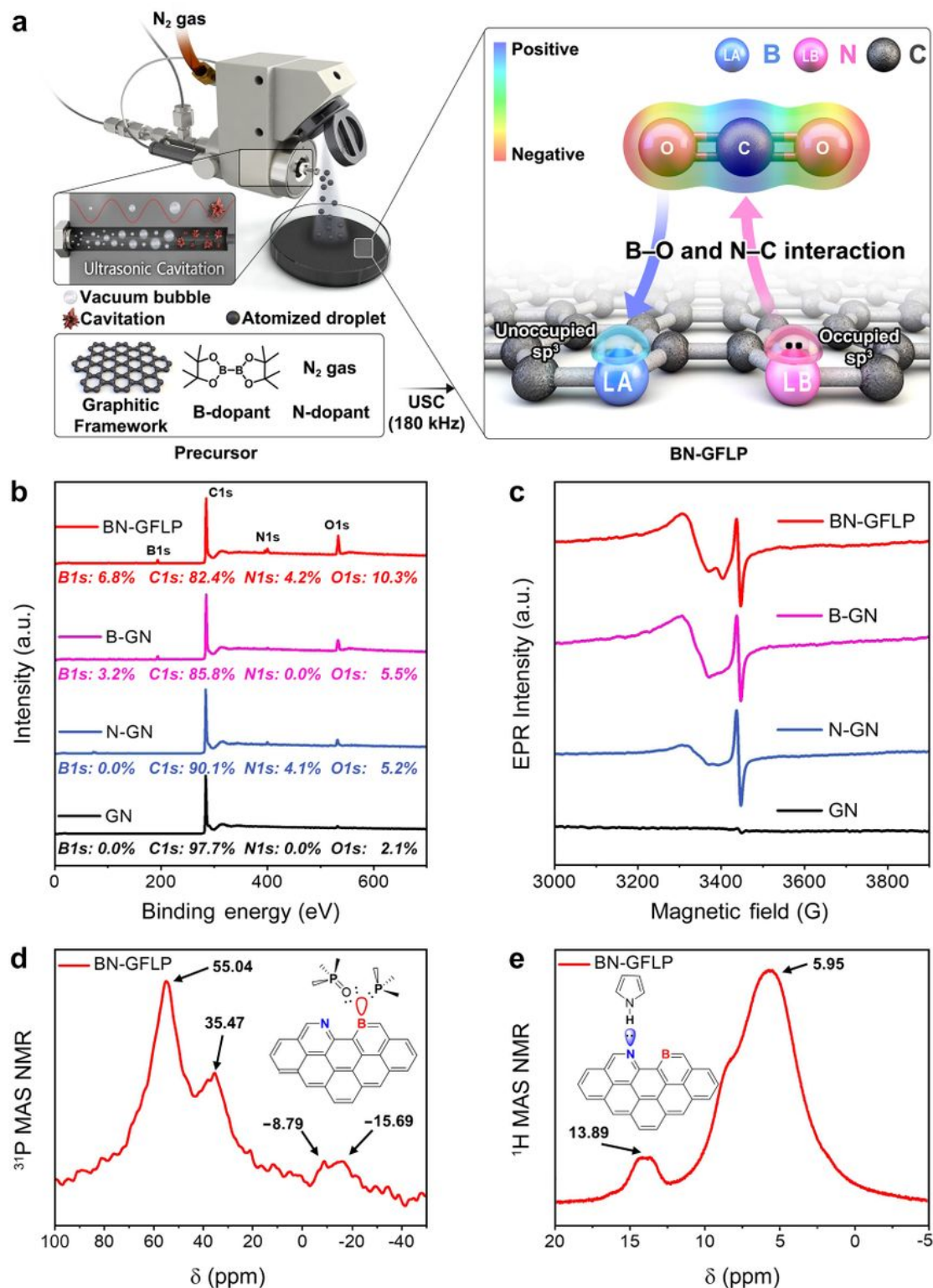


**Figure 1**

Sono-cavitation and nebulisation synthesis (SNS) process and BN-GFLP structure characterisation. (a) Schematic of the SNS process for BN-GFLP synthesis and molecular interactions between BN-GFLP and CO<sub>2</sub>. (b) Survey XPS spectra (normalised to C1s) and (c) EPR spectra of GN, N-GN, B-GN, and BN-GFLP at

10 K. (d)  $^{31}\text{P}$  MAS NMR spectrum of TMP on BN-GFLP. (e)  $^1\text{H}$  MAS NMR spectrum of pyrrole adsorbed on BN-GFLP.

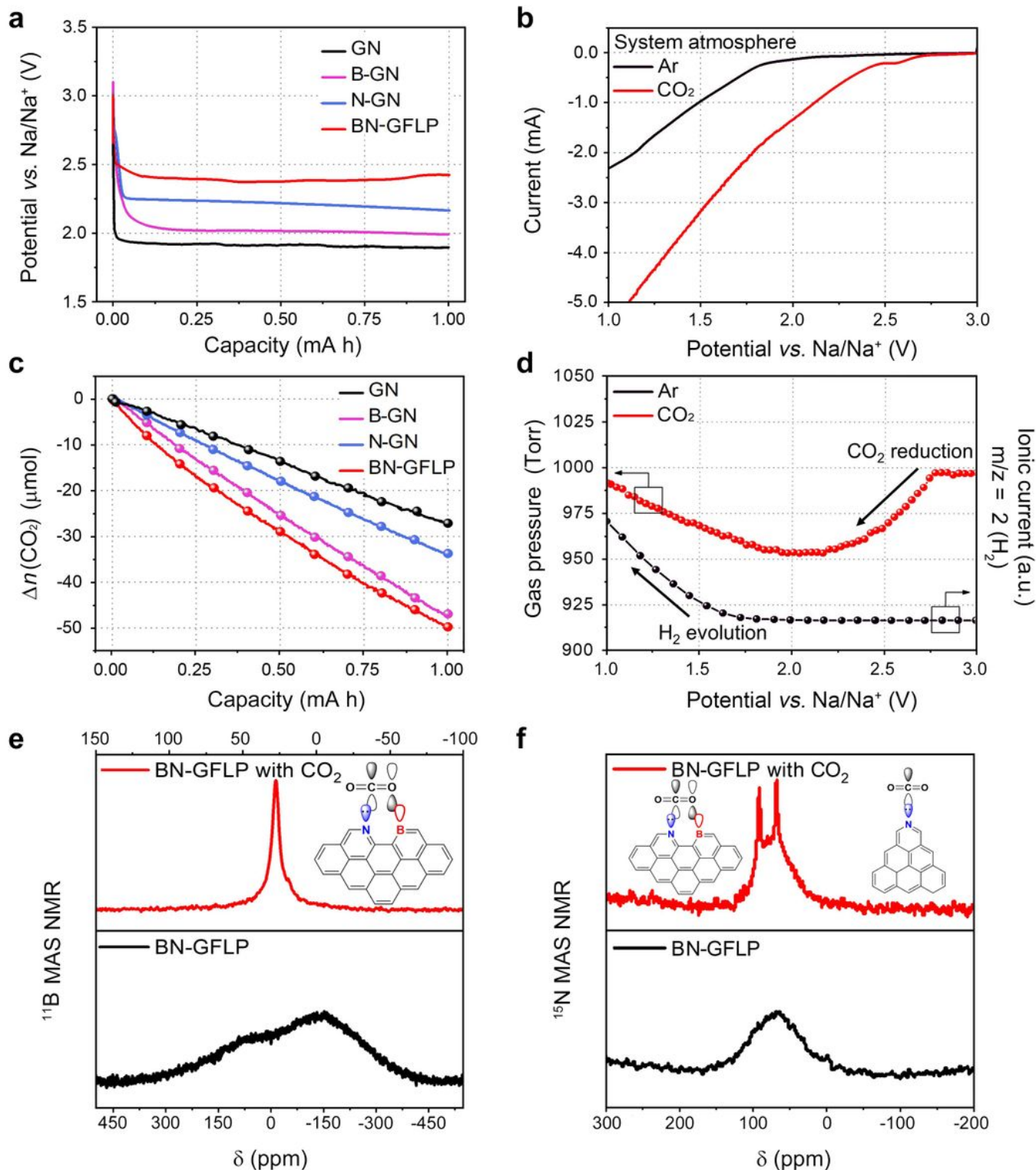


**Figure 2**

Electrochemical  $\text{CO}_2$  reduction on the BN-GFLP electrode in seawater. (a) Galvanostatic discharge voltage profiles of the CBS system with the prepared catalysts at a fixed current density of  $0.13 \text{ mA cm}^{-2}$  and (b) LSV profiles of the BN-GFLP catalyst under various system atmospheres in the 3.0–1.0 V voltage

window at a sweep rate of  $0.1 \text{ mV s}^{-1}$ . (c) Quantitative  $\text{CO}_2$  gas consumption during the galvanostatic discharge process in (a). (d) Inner pressure decay (red) and complementary DEMS (black) results corresponding to the LSV profiles in (b). (e) 11B and (f) 15N MAS NMR spectra of BN-GFLP with (red) and without (black)  $\text{CO}_2$  stimulus. Possible binding configurations between BN-GFLP and  $\text{CO}_2$  are shown in the insets of (e) and (f).

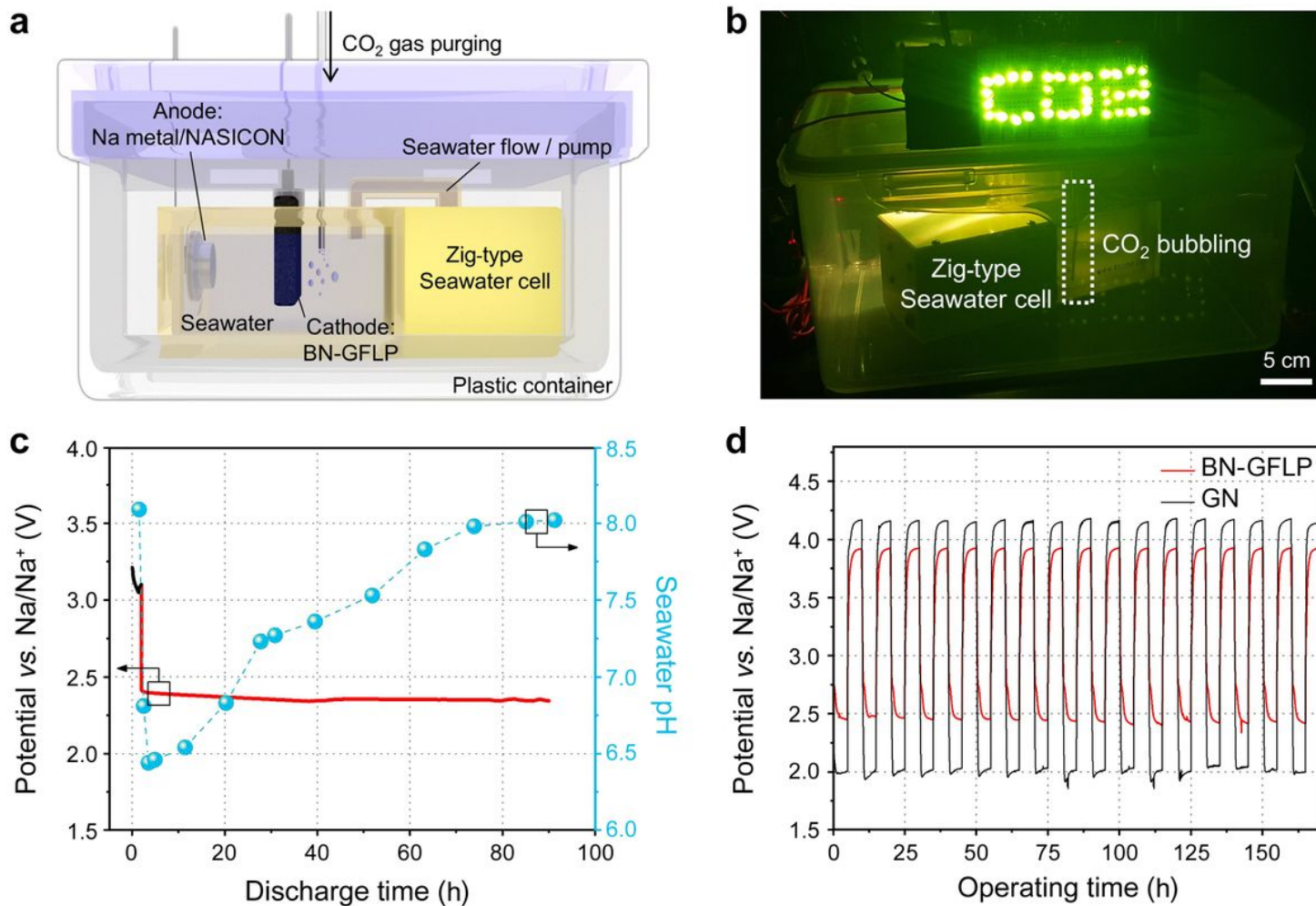


**Figure 3**

Electric energy harvesting and stability of the CBS system with the BN-GFLP cathode during  $\text{CO}_2\text{R}$ . (a) Schematic of the zig-type CBS system. (b) Digital photograph of 36 LEDs powered by the CBS system. (c) Seawater pH as a function of time during  $\text{CO}_2\text{R}$  with a fixed current density of  $0.13 \text{ mA cm}^{-2}$ . The pH was controlled by bubbling  $\text{CO}_2$  into the seawater. (d) Galvanostatic charge-discharge voltage plots of zig-type CBS cells with BN-GFLP and control GN cathodes.

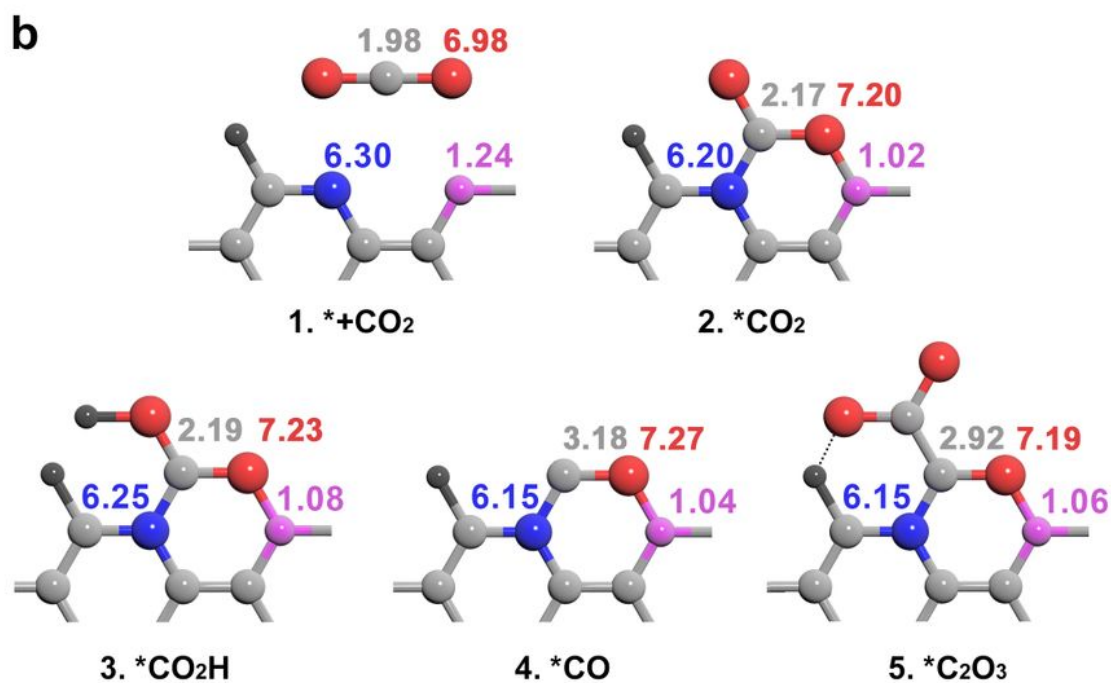
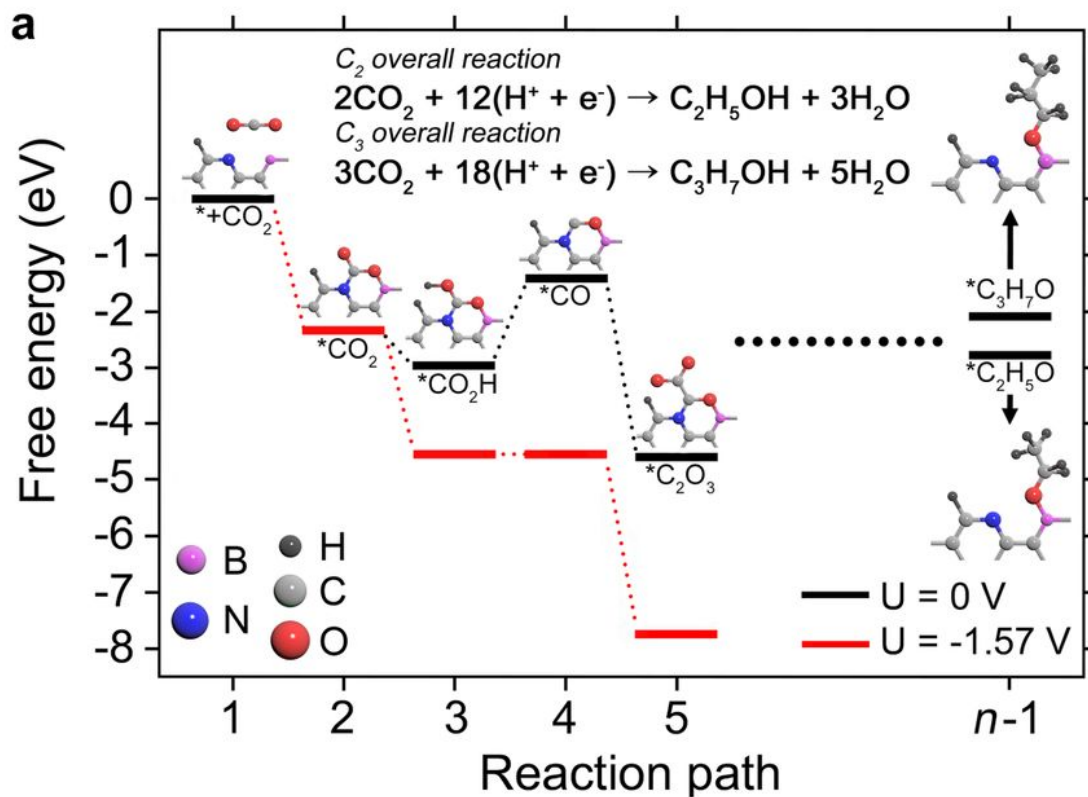


**Figure 4**

DFT calculations of the BN-GFLP catalyst for CO<sub>2</sub>R. (a) Gibbs free energy diagram for CO<sub>2</sub>R reaction to C<sub>2</sub>+ products on the BN-GFLP electrode. The red lines show the optimal mechanism for C<sub>2</sub>+ product formation at an applied potential of -1.57 V. According to the reaction path at 0 V applied potential (black lines) CO–CO<sub>2</sub> coupling (4 → 5) is highly favourable, with a Gibbs free energy difference of -3.2 eV. (b) Bader charges (e<sup>-</sup>) of the active sites in BN-GFLP and the reaction-path intermediates corresponding to

(a). The Bader charge of each atom is shown in in the same color as the corresponding atom: hydrogen (black), nitrogen (blue), boron (purple), carbon (grey), and oxygen (red).

## Supplementary Files

This is a list of supplementary files associated with this preprint. Click to download.

- [MovieS1.mp4](#)
- [SupplementaryInformation.docx](#)